

## Article

# Manipulating the electronic state of ruthenium to boost highly selective electrooxidation of ethylene to ethylene glycol in acid

Jie Wang <sup>a,b</sup>, Yihe Chen <sup>a,b</sup>, Yuda Wang <sup>b</sup>, Hao Zhao <sup>b</sup>, Jinyu Ye <sup>c</sup>, Qingqing Cheng <sup>b,\*</sup>, Hui Yang <sup>a,b,\*</sup><sup>a</sup> School of Physical Science and Technology, Shanghai Tech University, Shanghai 201210, China<sup>b</sup> Shanghai Advanced Research Institute, Chinese Academy of Sciences, Shanghai 201210, China<sup>c</sup> College of Chemistry and Chemical Engineering, Xiamen University, Xiamen 361005, Fujian, China

## ARTICLE INFO

## Article history:

Received 24 January 2024

Accepted 26 March 2024

Available online 20 May 2024

## Keywords:

Ethylene electrooxidation

Ethylene glycol

High selectivity

IrRu alloy

Electronic structure

## ABSTRACT

Electrochemical oxidation of ethylene is a novel approach to manufacture valuable ethylene glycol (EG), which is an important raw material in organic chemical industry. However, the poor EG selectivity and expensive additional purification costs hinder this method from being practically used. In this work, ultrafine iridium-ruthenium (IrRu) alloy nanoparticles are synthesized through the precipitation-reduction method and their electrocatalytic performance towards ethylene oxidation to EG has been comprehensively studied. Near 100% selectivity is achieved with a EG yield of 60.62 mmol g<sub>Ru</sub><sup>-1</sup> h<sup>-1</sup> at 1.475 V on an optimal Ir<sub>0.54</sub>Ru<sub>0.46</sub> catalyst. OH-stripping, *in-situ* electrochemical attenuated total internal reflectance Fourier transform infrared spectra and DFT calculation reveal that the introduction of Ir can modulate the electronic structure and *d*-band center so as to endow the Ru with the mild binding energy with the key intermediates and small energy barrier for \*HOCH<sub>2</sub>CH<sub>2</sub>OH desorption, thereby enhancing the EG generation. Simultaneously, the high energy barrier for the overoxidation of the \*CH<sub>2</sub>CH<sub>2</sub>OH renders the EG formation thermodynamically favorable, thus realizing the near 100% EG selectivity. This work provides a new understanding for the high-selectivity electrosynthesis of high-value-added oxides.

© 2024, Dalian Institute of Chemical Physics, Chinese Academy of Sciences.

Published by Elsevier B.V. All rights reserved.

## 1. Introduction

Ethylene glycol (EG) is an important bulk chemical due to its widespread applications in manufacturing industry [1,2]. Traditionally, EG is mainly produced from petroleum-derived ethylene [3], that commonly undergoes the epoxidation and hydrolysis processes [4]. However, this method always evolves the high temperature and pressure, along with using expensive oxidants (e.g., H<sub>2</sub>O<sub>2</sub>), which contradicts the principles of green chemistry [5,6]. Nowadays, with the rapid development of renewable electricity generation, electrosynthesis technique has

emerged as the sustainable and powerful route for chemicals production under ambient conditions. Thereinto, electrocatalytic anodic oxidation (EOA) can produce the value-added oxygenated chemicals only regulating the potentials and using water as the oxygen source, attracting the considerable attention [7,8]. Meanwhile, EOA could be coupled with cathodic reduction reactions (e.g., hydrogen evolution, CO<sub>2</sub> electroreduction, etc.), thereby achieving the goal of two birds with one stone [9–15]. Unfortunately, only a few studies have been focused on the EG synthesis through EAO to date. For example, early report has developed the silver (Ag) electrode [16], which

\* Corresponding author. E-mail: chengqq@sari.ac.cn (Q. Cheng), yangh@sari.ac.cn (H. Yang).

This work was supported by the National Key R&amp;D Program of China (2021YFB4000200) and the Shanghai Science and Technology Innovation Action Plan (23ZR1471000).

[https://doi.org/10.1016/S1872-2067\(24\)60024-0](https://doi.org/10.1016/S1872-2067(24)60024-0)

can catalyze the conversion of ethylene to EG at the anode. However, the current density is extremely low (microampere level) and the Faraday efficiency (FE) is too small to be quantified. Until recently, Sargent *et al.* [6] have designed the Au-doped Pd catalyst that can realize the electrosynthesis of EG from ethylene with milliamperes level and 80% FE in alkaline medium, representing an important step in such a field. Nevertheless, multiple products still be detected in the above system, including formic acid, oxirane, glycolaldehyde, glycolic acid, and the selectivity of EG is only 60%, which necessarily requires the tedious post-processing steps, including separation and purification. Therefore, how to improve the selectivity of EG is especially important for the EG electrosynthesis.

As the literature demonstrated, ethylene-to-EG conversion involves the transfer of two \*OH intermediate, thus the selectivity of EG is strongly associated with the adsorption energy between \*OH intermediate and active site. Although a few studies have been devoted to adjusting the \*OH binding energy, the issues in diversity of products and selectivity of EG are still not addressed yet [17,18]. Design of new material with appropriate \*OH binding energy is thus imperative. Pt-group catalysts have been proved to efficiently catalyze the oxidation of olefins to various oxygenated chemicals [6,16–21]. Among them, Ru might be a suitable candidate for efficient electrooxidation of ethylene to EG since it has a moderate \*OH binding energy [22], which favors for the desorption of \*OH to form EG. Beyond that, the rich electron of  $\pi$  bond for ethylene and the unfilled 4d orbitals of Ru also make the ethylene molecular easily adsorb onto the Ru surface, thereupon facilitating the activation of ethylene. However, Ru exhibits the poor durability during the EAO process, especially operation in acidic electrolyte, which imposes a formidable challenge to efficiently catalyze conversion of ethylene to EG [23,24].

Herein, we propose an alloying strategy between Ir and Ru to promote the selectivity and durability [25–28] in the electrooxidation of ethylene to EG. It is found that the prepared IrRu alloy with appropriate Ir/Ru ratio (i.e.,  $\text{Ir}_{0.54}\text{Ru}_{0.46}$ ) can achieve nearly 100% EG selectivity while attaining the excellent durability, which is far better than the Ru-NPs counterpart with low selectivity (43.8%) and poor durability. Advanced spectroscopies reveal that alloying Ir makes Ru positively charged, thus weakening the \*OH adsorption. OH-stripping experiment confirms that \*OH is more easily desorbed from Ru site as the increase in Ir/Ru atomic ratio, which facilitates the coupling of \*OH and ethylene. In addition, free radical quenching and D-labeled isotope experiments verify that ethylene-EG conversion on IrRu catalyst is not tandem but direct electrocatalytic reaction with the \*OH-transfer as the rate-determining step. *In-situ* infrared spectroscopy clarifies that the ethylene is activated on Ru site through Pauling-type adsorption configuration. Simultaneously, only  $^{*}\text{CH}_2\text{CH}_2\text{OH}$  intermediate without other oxygen groups (epoxy group) can be detected, proving the no occurrence of overoxidation. DFT calculation further corroborates that alloying with Ir not only accelerates the \*OH transfer but also optimizes the reaction pathway, making the EG selectivity close to 100%. This work offers a new design perspective to develop the high selectivity electrocatalyst for

electrosynthesis of EG from ethylene.

## 2. Experimental

### 2.1. Synthesis of Ru NPs and IrRu alloys

The synthesis of  $\text{Ir}_{0.57}\text{Ru}_{0.43}$  NPs was accomplished using the precipitation-reduction method as follows: 274.5 mg of  $\text{H}_2\text{IrCl}_6\cdot x\text{H}_2\text{O}$  (Scrc), 68.25 mg of  $\text{RuCl}_3\cdot x\text{H}_2\text{O}$  (Titan), and 400 mg of  $\text{MgO}$  (Scrc) were dissolved in 150 mL of deionized water (resistivity  $18.2 \text{ M}\Omega \text{ cm}^{-1}$ , Titan) under magnetic stirring, resulting in a brown solution with white suspended particles. Next, 15 mL of 0.5 mol  $\text{L}^{-1}$  KOH was added to the mixed solution to adjust the pH to 10.0, measured using a pH meter. The mixture solution was transferred to a water bath, stirred, and heated to 90 °C for 3 h. Then, the obtained colloidal Ir and Ru suspension was centrifuged, sonicated, and washed with deionized water, repeating this process three times until the filtrate became clear and transparent. Subsequently, the precipitate was dried at 60 °C in a vacuum oven overnight. The powder was finely ground in an mortar and placed into a ceramic crucible. Afterwards, the powder was heated under argon gas at a rate of  $10 \text{ }^{\circ}\text{C min}^{-1}$  to 350 °C and maintained for 2 h under 10 vol%  $\text{H}_2\text{-Air}$  gas. The obtained powder was treated in 0.5 mol  $\text{L}^{-1}$   $\text{H}_2\text{SO}_4$  solution at room temperature for 1 h and centrifuged for three times with water. After vacuum drying at 60 °C for 8 h, the final IrRu alloy catalyst was prepared.

The synthesis of  $\text{Ir}_{0.54}\text{Ru}_{0.46}$ ,  $\text{Ir}_{0.46}\text{Ru}_{0.54}$  NPs follows the same procedure only changing the Ir/Ru molar ratios to 1:1, 0.5:1, respectively. Ru NPs are also prepared under the same procedure in the absence of Ir precursor.

### 2.2. Electrode preparation

Typically, 2 mg of catalyst and 20  $\mu\text{L}$  of a 5 wt% Nafion solution are sonicated to form a suspension in 0.5 mL ethanol. Next, 25  $\mu\text{L}$  of the ink is uniformly spread onto a carbon paper with dimensions of 0.5 cm  $\times$  2 cm. The prepared electrode is then dried for future use. The active area is 0.5  $\times$  0.5 cm<sup>2</sup>.

### 2.3. Characterization

X-ray diffraction (XRD) patterns were recorded by using a Philips X'Pert Pro Super diffractometer with  $\text{Cu K}\alpha$  radiation ( $\lambda = 1.54178 \text{ \AA}$ ). The X-ray photoelectron spectroscopy (XPS) spectra were recorded on a Thermo ESCALAB250Xi spectrometer with an excitation source of monochromatized Al  $K\alpha$  ( $h\nu = 1486.6 \text{ eV}$ ) and a pass energy of 30 eV. The values of binding energies were calibrated with the C 1s peak of contaminant carbon at 284.80 eV. Electrochemical impedance spectroscopy (EIS) was tested in frequency from 1 Hz to 1000 kHz with 5 mV amplitude at 1.4 V (vs. RHE).

### 2.4. Electrochemical ethylene oxidation and product analysis

Electrochemical measurements are conducted using CHI-760E instrument (Shanghai Ch Instrument Co. Ltd). Ex-

periments are conducted in a H-cell with a 50 mL electrolyte volume in both anode and cathode chambers. Pt foil and Hg/Hg<sub>2</sub>SO<sub>4</sub> served as the counter and reference electrodes, respectively. The electrolyte is 0.1 mol L<sup>-1</sup> HClO<sub>4</sub>, and a Nafion 115 membrane was employed to separate the cathode and anode chambers. Ethylene gas is continuously supplied at a constant flow rate of 15 mL min<sup>-1</sup> into the anode chamber using a mass flow controller. The reported potentials are calibrated against RHE using the following equation:

$$E(\text{RHE}) = E(\text{Hg/Hg}_2\text{SO}_4) + 0.205 + \text{pH} \times 0.0591$$

Current densities are reported based on the geometric electrode area. Product quantification is performed using <sup>1</sup>H NMR spectroscopy with water suppression techniques. The internal standard is dimethyl sulfoxide (DMSO), and D<sub>2</sub>O is served as the lock solvent.

### 3. Results and discussion

#### 3.1. Structural characterizations of IrRu alloy catalyst

Different ratios of IrRu alloy nanoparticles (NPs) were prepared using the precipitation-reduction method by adding different proportions (H<sub>2</sub>IrCl<sub>6</sub>·xH<sub>2</sub>O, RuCl<sub>3</sub>·xH<sub>2</sub>O, MgO) of Ir and Ru precursors (Fig. 1(a)). The real atomic ratios of the three IrRu samples were determined to be Ir<sub>0.57</sub>Ru<sub>0.43</sub>, Ir<sub>0.54</sub>Ru<sub>0.46</sub> and Ir<sub>0.46</sub>Ru<sub>0.54</sub>, respectively, by using ICP-OES alkali fusion method (Table S1). XRD patterns of three IrRu samples (Fig. 1(b)) show that the characteristic peak gradually shifts to low angle with an increase in Ir/Ru ratio, indicative of the lattice tensile strain after alloying with Ir atoms. Upon comparing with standard PDF cards (#65-5982 for HCP, #65-5546 for FCC), it is apparent that an increase in Ir content results in the transformation

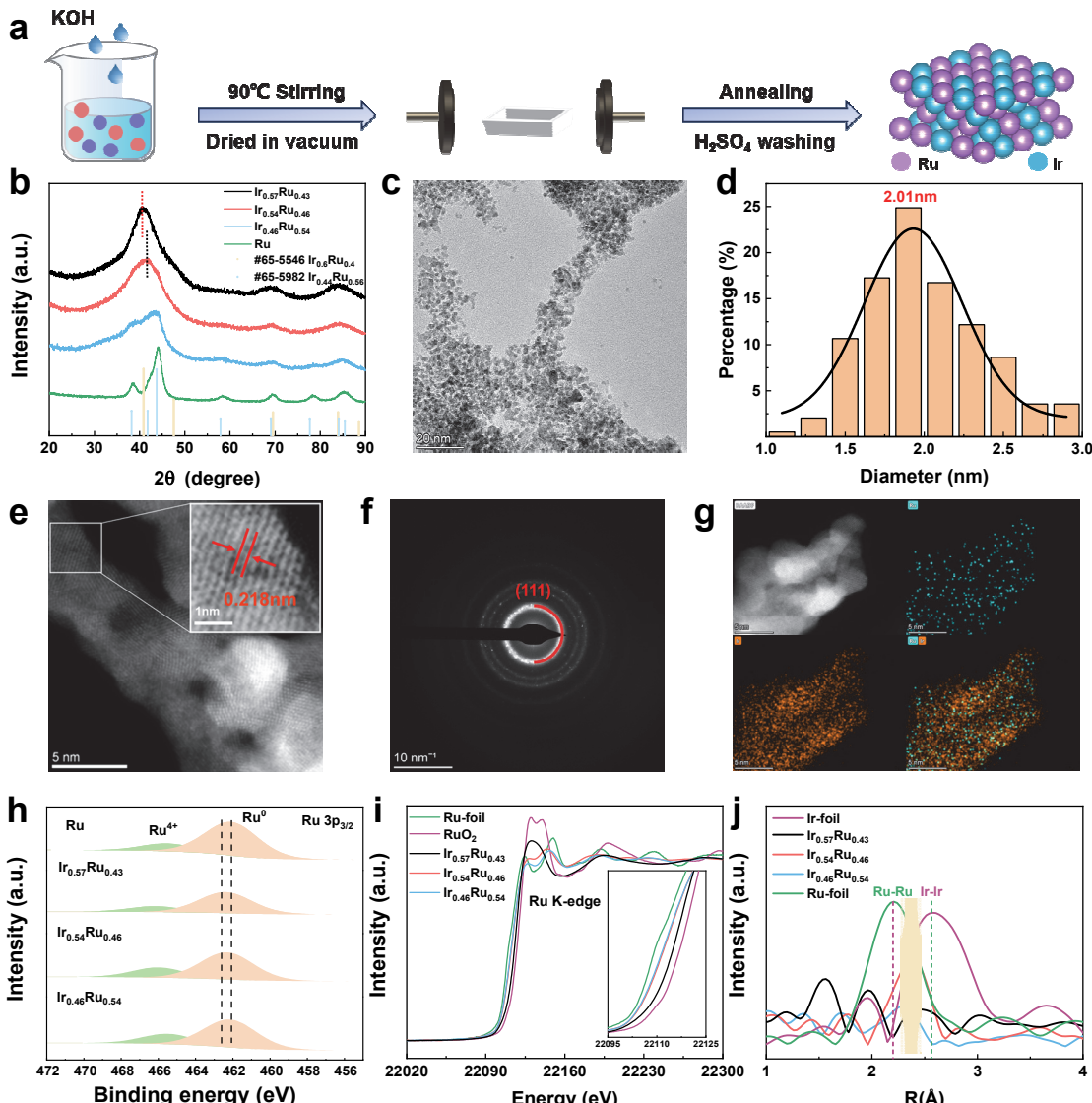


**Fig. 1.** Synthetic scheme and characterization of Ir-Ru NPs. (a) Schematic illustration of the synthetic process. (b) XRD patterns of Ir<sub>0.57</sub>Ru<sub>0.43</sub>, Ir<sub>0.54</sub>Ru<sub>0.46</sub>, Ir<sub>0.46</sub>Ru<sub>0.54</sub> and Ru NPs. TEM image (c) and alloy nanoparticle size distribution (d) of Ir<sub>0.54</sub>Ru<sub>0.46</sub> NPs. Aberration STEM image (e), SAED pattern (f) and elemental mapping (g) for Ir<sub>0.54</sub>Ru<sub>0.46</sub> NPs. (h) High-resolution XPS spectra of Ru 3p<sub>3/2</sub>. Normalized XANES (i) and R-space of the EXAFS spectra (j) of Ir<sub>0.57</sub>Ru<sub>0.43</sub>, Ir<sub>0.54</sub>Ru<sub>0.46</sub>, Ir<sub>0.46</sub>Ru<sub>0.54</sub>, Ir foil, and Ru foil at the Ru K-edge.

of the alloy from the HCP structure of  $\text{Ir}_{0.46}\text{Ru}_{0.54}$  to the FCC structure of  $\text{Ir}_{0.57}\text{Ru}_{0.43}$  and  $\text{Ir}_{0.54}\text{Ru}_{0.46}$  [29,30]. TEM images (Figs. 1(c) and S1) demonstrate the uniformly dispersed Ir-Ru-NPs with an average size of ca. 2 nm (Fig. 1(d)). High-resolution STEM images (Figs. 1(e) and S2) display that the lattice spacings are ca. 0.206, 0.218 and 0.226 nm corresponding to the (101) plane of  $\text{Ir}_{0.46}\text{Ru}_{0.54}$ , (111) plane of  $\text{Ir}_{0.54}\text{Ru}_{0.46}$  and (111) plane of  $\text{Ir}_{0.57}\text{Ru}_{0.43}$ -NPs respectively, attesting the tensile lattice, which matches well with the XRD results. This can also be confirmed by the selected area electron diffraction (SAED) pattern (Figs. 1(f) and S3). Besides, the EDS-mapping (Fig. 1(g) and S4) represents the homogeneous dispersion of Ir and Ru elements over the small-sized NPs, proving the high alloying state for the prepared IrRu catalyst.

XPS survey spectra (Fig. S5, Table S2) show the existence of O, Ir and Ru atoms on the surface of IrRu alloy. In particular, Ru 3p<sub>3/2</sub> XPS spectra (Fig. 1(h)) show that the Ru(0) peak shifts to high binding energy after the alloying with Ir, indicative of the positively charged for the Ru atoms. X-ray absorption near-edge structure (XANES) was performed to further investigate the electronic state and local coordination of Ru atoms.

The Ru K-edge XANES (Fig. 1(i)) shows that the absorption-edge energy of IrRu-alloys is higher than that of the Ru-foil, again demonstrating the electron transfer from Ru to Ir, which is consistent with the XPS analyses. Fig. 1(j) shows the extended X-ray absorption fine structure (EXAFS) spectra at Ru k-edge for  $\text{Ir}_{0.57}\text{Ru}_{0.43}$ ,  $\text{Ir}_{0.54}\text{Ru}_{0.46}$ ,  $\text{Ir}_{0.46}\text{Ru}_{0.54}$ , and Ru foil. The IrRu alloys exhibit the dominant peaks, which are situated between Ru-Ru and Ir-Ir bonds, probably attributing to the formation of Ir-Ru bond. Meanwhile, the fitting results (Fig. S6 and Table S3.) reveal that the bond lengths increase from 2.66 to 2.74 Å and the coordination number of Ru-Ir also increases from 5.8 to 7.8, with the increase in Ir content, indicative of the regulated local coordination structure of Ru after the introduction of Ir [31,32].

### 3.2. Electrooxidation of ethylene to EG on IrRu alloy catalysts

Electrooxidation of ethylene to EG was conducted in ethylene-saturated 0.1 mol L<sup>-1</sup>  $\text{HClO}_4$  solution and the oxygen evolution reaction (OER) is the main competing reaction [11,33]. By comparing the CVs of IrRu alloy (Fig. 2(a)) under  $\text{N}_2$

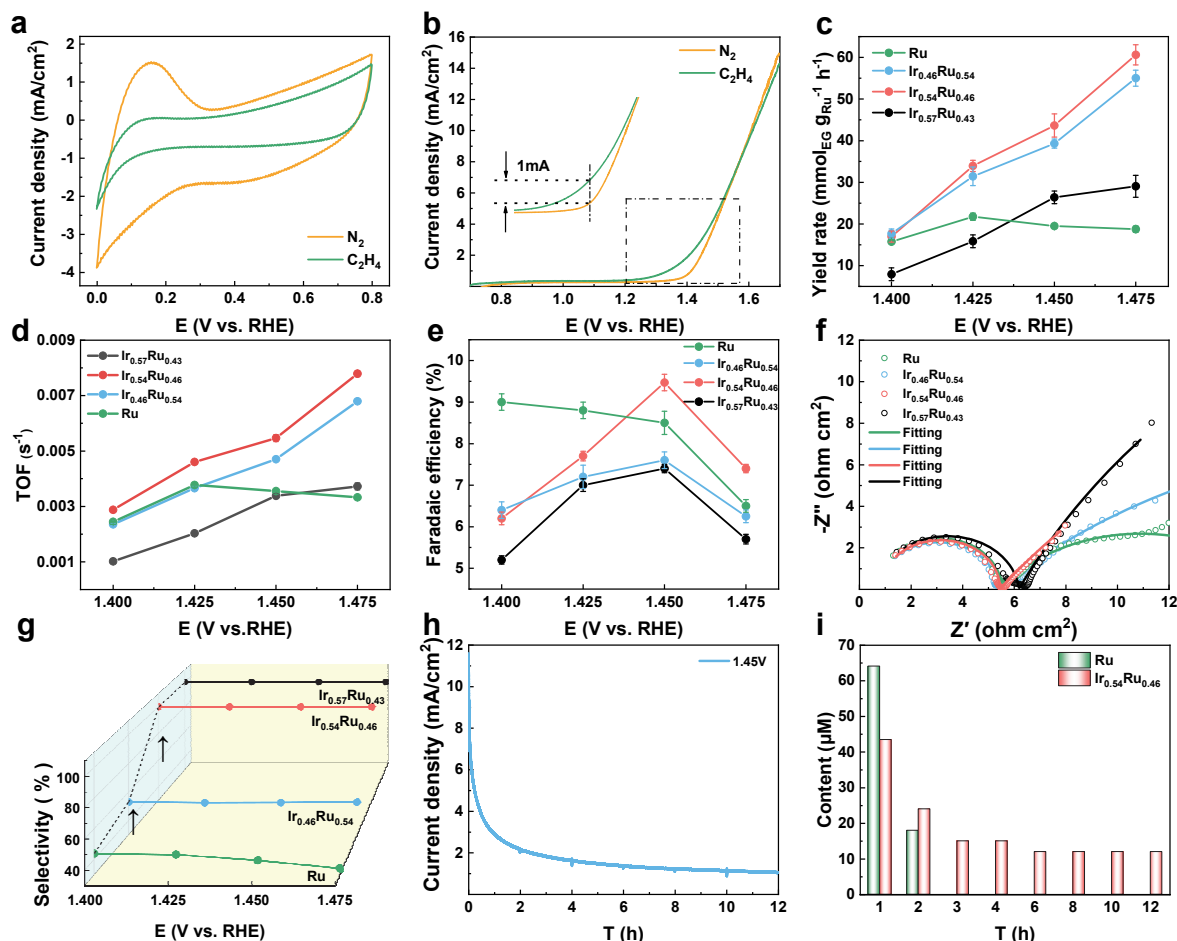


**Fig. 2.** Catalytic performance of IrRu alloy NPs and Ru NPs toward ethylene to EG in 50 mL 0.1 mol L<sup>-1</sup>  $\text{HClO}_4$ . CVs (a) and LSVs (b) of  $\text{Ir}_{0.54}\text{Ru}_{0.46}$  NPs in  $\text{N}_2$ - and ethylene-saturated electrolyte. Yield rates of EG (c), TOF (d) and  $\text{FE}_{\text{EG}}$  (e) at the potentials from 1.400 to 1.475 V. (f) Nyquist plots of different catalysts (The inset is equivalent circuit, where  $R_s$ ,  $R_c$ ,  $C_c$ ,  $C_{dl}$  and  $R_{ct}$  represent electrolyte resistance, contact resistance, contact capacitance, Double-layer capacitance and charge transfer resistance, respectively). (g) Selectivity of EG at a potential range from 1.400 to 1.475 V. (h) Durability test for  $\text{Ir}_{0.54}\text{Ru}_{0.46}$  NPs. (i) EG productivity rate at 1.45 V during the 12 h electrolysis.

and ethylene, it is found that the areas of the hydrogen underpotential deposition ( $UPD_H$ ) region under saturated ethylene significantly decrease in comparison with that under  $N_2$  condition, signifying the adsorption of ethylene molecular on the active sites, which is the prerequisite for the electrooxidation of ethylene. The linear sweep voltammetry (LSV) curves of various catalysts (Fig. 2(b) and Fig. S7) show that the current density is higher than that measured under  $N_2$  in the potential window of 1.20 to 1.59 V, assessing that the oxidation of ethylene predominately occurs at this potential range.

Control-potential electrolysis (CPE) at the potential range from 1.400 to 1.475 V was performed in the H-type electrolysis cell (Fig. S8), and the chronoamperometric data of electrolysis were recorded in Fig. S9. The products after CPE were analyzed by  $^1H$  nuclear magnetic resonance ( $^1H$ -NMR) spectroscopy and gas chromatography (GC). As shown in Fig. S10, EG can be detected after 2 h electrolysis at 1.400 to 1.475 V on IrRu alloys and Ru NPs catalysts while no EG is detected on pure Ir NPs (Figs. S11 and S12), implying that the Ru atoms are the real active sites for the ethylene electrooxidation. It is noting that, the formic acid and glycolic acid are produced on the Ru NPs and  $Ir_{0.46}Ru_{0.54}$  NPs while those cannot be formed on the  $Ir_{0.54}Ru_{0.46}$  NPs and  $Ir_{0.57}Ru_{0.43}$  NPs, demonstrating that the high Ir ratio is beneficial to realize the conversion of ethylene to EG. Notably, no CO and  $CO_2$  were detected in the GC data (Fig. S13) for any catalyst, signifying the absence of gaseous by-products in this reaction. The corresponding EG yield on various catalysts at different potentials is depicted in Fig. 2(c). The EG yield distribution on Ru NPs displays a volcano-type trend that depends on the applied potentials. The highest yield can be achieved at a potential of 1.425 V with a value of 21.75 mmol  $Ru^{-1} h^{-1}$ . However, the EG yields of IrRu alloys monotonically increase with raising the potential and their respective maximum yields are 29.05, 60.62, and 55.02 mmol  $g_{Ru}^{-1} h^{-1}$  at a potential of 1.475 V for  $Ir_{0.46}Ru_{0.57}$ ,  $Ir_{0.54}Ru_{0.46}$  and  $Ir_{0.57}Ru_{0.43}$  NPs. Obviously, the  $Ir_{0.54}Ru_{0.46}$  shows the highest EG yield, demonstrating that the moderate Ir/Ru could obtain the optimal performance for ethylene-to-EG conversion. To accurately calculate the turnover frequency (TOF) of EG production for each catalyst, we employed the copper underpotential deposition (Cu-UPD) method to determine the sites of Ru (Fig. S14, table S4). The  $Ir_{0.54}Ru_{0.46}$  NPs also delivers the highest turnover frequency (TOF, Fig. 2(d)) of EG among the IrRu alloys at each potential. In particular, at 1.475 V,  $Ir_{0.54}Ru_{0.46}$  NPs catalyst exhibits the highest TOF ( $0.0078 s^{-1}$ ), which is 2.1, 1.1 and 2.2 times higher than those of  $Ir_{0.57}Ru_{0.43}$  NPs ( $0.0037 s^{-1}$ ),  $Ir_{0.46}Ru_{0.57}$  NPs ( $0.0068 s^{-1}$ ) and Ru NPs ( $0.0033 s^{-1}$ ), respectively, again indicative of its high intrinsic activity towards electrooxidation of ethylene to EG (Fig. S15, Table S5). Faradaic efficiency of EG ( $FE_{EG}$ , Fig. 2(e)) on Ru NPs catalyst displays an inverse relationship with the applied potential and a significant decrease in  $FE_{EG}$  (from 8.5% to 6.5%) is observed in the potential range of 1.450–1.475 V, probably attributing to the overoxidation of ethylene under the high working potentials. On the contrary, after alloying with Ir, the  $FE_{EG}$  on IrRu alloys show a volcano-shaped relationship and reach a peak value at 1.45 V. Noteworthily,  $Ir_{0.54}Ru_{0.46}$  NPs catalyst delivers the higher  $FE_{EG}$

(9.5%) than those of  $Ir_{0.57}Ru_{0.43}$  NPs (7.6%) and  $Ir_{0.46}Ru_{0.54}$  NPs (7.4%). Excessively high or low Ir/Ru ratio is detrimental to the improvement of  $FE_{EG}$ . EIS spectra (Fig. 2(f), Table S6) represent the gradual increase of semicircles ( $R_{ct}$ ) as the increase in the proportion of Ir. Considering the OER plays a dominant role in anodic oxidation reaction, we hold the opinion that the introduction of Ir is conducive to inhibiting the OER kinetics, which can also interpret the enhanced FE on IrRu alloys.

In addition to the activity improvement, the product distribution (i.e., selectivity of EG) is also optimized after alloying with Ir. As shown in Fig. S16, the highest selectivity of EG on Ru NPs is 43.8% at a potential of 1.4 V accompany with other by-products, as evidenced by Fig. 2(g). This finding suggests that the ethylene electrooxidation on Ru NPs prefers to generate the oxidative byproducts, such as glycolic acids, other than the EG. Interestingly, the introduction of Ir to form  $Ir_{0.46}Ru_{0.54}$  NPs can improve the EG selectivity from 43.8% to 52.9% (Fig. 2(g)), and the selectivity remains stable as the increase in applied potential. Further elevating the Ir ratio can dramatically promote the EG selectively up to 100% for  $Ir_{0.54}Ru_{0.46}$  NPs and  $Ir_{0.57}Ru_{0.43}$  NPs catalysts at the wide potential window without any other byproducts, standing at the forefront of current research (Table S7). Above results clearly elucidate the positive effectiveness of Ir alloying on the highly selective electrosynthesis of EG.

Durability test (12 h-electrolysis under 1.45 V) was performed on the optimal  $Ir_{0.54}Ru_{0.46}$  NPs and Ru NPs catalysts, as shown in Fig. 2(h). Although the Ru NPs catalyst exhibits a higher current density than that on the  $Ir_{0.54}Ru_{0.46}$  NPs at the initial 6000 seconds (Fig. S17), it undergoes the severe attenuation after durability test. Notably, the EG is almost undetectable only after the 3 h-electrolysis (Fig. 2(i)), further confirming the poor durability of Ru NPs. In contrast,  $Ir_{0.54}Ru_{0.46}$  NPs shows a rapid decline in EG concentration during the first 6 h-electrolysis and remains stable with a productivity of ca. 6  $\mu\text{mol L}^{-1} h^{-1}$ . Particularly, the  $Ir_{0.54}Ru_{0.46}$  NPs after durability test shows a core-shell structure with a Ir-rich shell, indicative of the structural reconstruction during the EAO process, which is directly evidenced by the energy loss spectroscopy (EELS) (Fig. S18). Besides, XPS and EDS-mapping were carried out to investigate the variation of structure after the durability test. As shown in Fig. S19 and Table S8, the XPS survey spectra show an obviously reduced Ru atoms after the durability test, confirming the dissolution of Ru atoms. Simultaneously, the Ru  $3p_{3/2}$  XPS shows a similar valence state composition compared to the initial one (Fig. S20). EDS-mapping (Fig. S21) also reveal the reducing Ru atom during the EOR process, interpreting the performance degradation. It is noting that the calculated TOF after the durability test is similar to that of the initial catalyst (Fig. S22), demonstrating the intrinsic activity is not influenced after the formation of core-shell structure that is the precondition for the subsequent computational modeling.

### 3.3. Mechanism investigation

Before investigating the reaction mechanism of ethylene-EG conversion, we need to identify whether this reaction is a direct electrocatalytic route or free reactive oxygen species in the

electrolyte (ROS, ·OH, ·O<sup>2-</sup>, H<sub>2</sub>O<sub>2</sub>) [34,35] mediated tandem reaction. The ·OH and ·O<sup>2-</sup> species can be detected during the electrolysis, as shown in Fig. S23. Methanol and p-benzoquinone are chosen as the quenching agent due to their rapid reaction rates with ·OH and ·O<sup>2-</sup> radicals, respectively [5,36]. Both *i-t* and CV curves under ethylene atmosphere before and after addition of 100 mmol methanol or 100 mmol p-benzoquinone are identical (Fig. S24), confirming that the quenching agents cannot modify the surface structure of electrode. Subsequently, electrolysis under ethylene is performed in presence of methanol and p-benzoquinone. As shown in Fig. 3(a), the EG yield and FE<sub>EG</sub> are almost unchanged as comparison with those without addition of the quenching agents, corroborating that the ethylene-EG catalysis is not a ROS-mediated tandem reaction but a direct catalysis process.

The isotope D-labeling experiment (Fig. S25) shows that the molecular weight of EG changes from 63.04 (HOC<sub>2</sub>H<sub>4</sub>OH) to 65.09 (DOC<sub>2</sub>H<sub>4</sub>OD), signifying that the OH of EG is totally originated from the water [6]. Moreover, the OH-stripping experiment [37] (Fig. 3(b)) demonstrates that the desorption peak of surface \*OH intermediate displays a positive shift from 0.80 V (Ir<sub>0.46</sub>Ru<sub>0.54</sub>) to 0.86 V (Ir<sub>0.54</sub>Ru<sub>0.46</sub>) and 0.89 V (Ir<sub>0.57</sub>Ru<sub>0.43</sub>), respectively, indicating that the binding energy of \*OH (BE<sub>\*OH</sub>) decreases with an increase in Ir/Ru ratio. XPS valence band

spectroscopy (VBS) was performed to clarify the impact of Ir alloying on the *d*-band center of catalyst [38]. As shown in Fig. 3(c), the *d*-band center of catalyst gradually downshifts after increasing the proportion of Ir, also confirming that the introduction of Ir is beneficial to weaken the adsorption of key intermediates (e.g., \*OH), on the active sites. Previous reports have demonstrated that lowering BE<sub>OH</sub> can facilitate the transfer of \*OH to ethylene and hence the promoted activity [17,39,40].

Electrochemical in situ ATR-FTIR spectroscopy was further conducted on Ir<sub>0.54</sub>Ru<sub>0.46</sub>-NPs catalyst in ethylene-saturated 0.1 mol L<sup>-1</sup> HClO<sub>4</sub> to sensitively monitor the surface adsorbates during the EAO process. As shown in Fig. 3(d), the absorption peaks appear at 1655 and 1468 cm<sup>-1</sup>, which belong to the stretching vibration of the C=C bond ( $\delta_{\mu-C=C}$ ) and to the bending vibration of the C-H bond ( $\nu_{C-H}$ ), respectively, implying that the ethylene is adsorbed on the active site by Pauling adsorption configuration [41] (Table S9). Meanwhile, the intensities of the two absorption peaks gradually increase with potential, demonstrating that the high potential is beneficial for the activation of ethylene. The peak at 3475 cm<sup>-1</sup> is assigned as the OH stretching vibration ( $\delta_{O-H}$ ) mode adsorbed on Ru [42]. As the potential increases to 0.6 V, the intermediate species (e.g., \*CH<sub>2</sub>CH<sub>2</sub>OH) is observed at 3260 cm<sup>-1</sup>, which is formed through

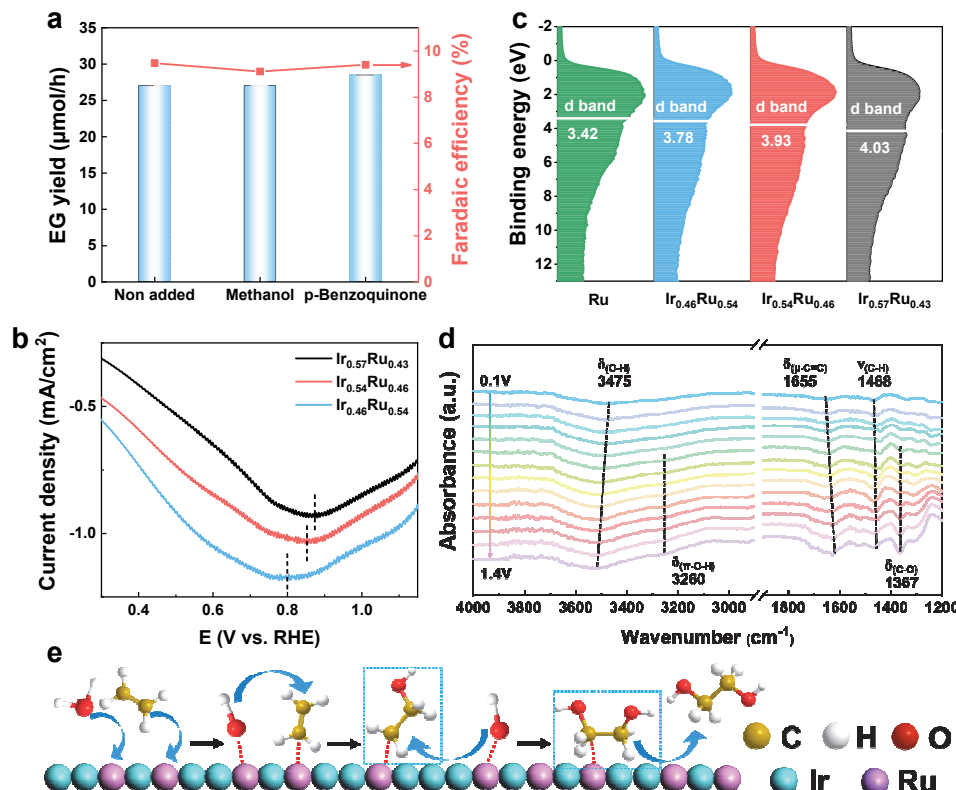


**Fig. 3.** (a) EG yielding and corresponding FE<sub>EG</sub> in the presence of 100 mmol methanol or 100 mmol p-benzoquinone of Ir<sub>0.54</sub>Ru<sub>0.46</sub> NPs catalysts, respectively. (b) Desorption of OH on Ir<sub>0.46</sub>Ru<sub>0.54</sub> NPs, Ir<sub>0.54</sub>Ru<sub>0.46</sub> NPs, Ir<sub>0.57</sub>Ru<sub>0.43</sub> NPs. CV curves with the scan rate of 50 mV s<sup>-1</sup>. (c) VBS of Ir<sub>0.57</sub>Ru<sub>0.43</sub>, Ir<sub>0.54</sub>Ru<sub>0.46</sub>, Ir<sub>0.46</sub>Ru<sub>0.54</sub>, and Ru NPs catalysts measured by XPS. (d) Electrochemical *in situ* ATR-FTIR spectra of ethylene oxidation on Ir<sub>0.54</sub>Ru<sub>0.46</sub> NPs at different potentials (0.1–1.4 V) in ethylene-saturated 0.1 mol L<sup>-1</sup> HClO<sub>4</sub> solution. (e) Schematic diagram of electrooxidation of ethylene to EG on IrRu alloy.

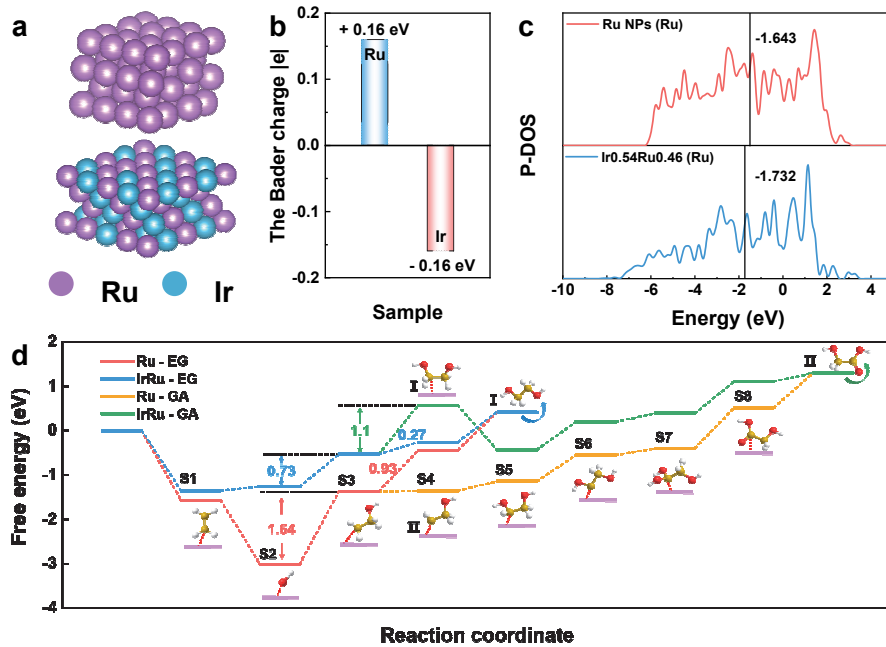


**Fig. 4.** Theoretical calculations for ethylene oxidation. (a) Calculation model for Ru NPs and Ir<sub>0.54</sub>Ru<sub>0.46</sub> NPs. (b) Charge transfer between Ir and Ru atoms in Ir<sub>0.54</sub>Ru<sub>0.46</sub> NPs. (c) P-DOS for Ru NPs and Ir<sub>0.54</sub>Ru<sub>0.46</sub> NPs. (d) Free energy diagram on Ru NPs and Ir<sub>0.54</sub>Ru<sub>0.46</sub> NPs (pathway I: C<sub>2</sub>H<sub>4</sub> → HOCH<sub>2</sub>CH<sub>2</sub>OH, pathway II: C<sub>2</sub>H<sub>4</sub> → HOCH<sub>2</sub>COOH).

the coupling of \*OH and the activated ethylene on the surface (Fig. S26). Notably, the conjugation effect of the C=C bond leads to a red-shift in the absorption peak of the OH group ( $\delta_{\text{H-O-H}}$ ), making it shift from 3475 to 3260 cm<sup>-1</sup>. Meanwhile, the \*CH<sub>2</sub>CH<sub>2</sub>OH intermediate peak reaches the maximum intensity at 1.2 V and stabilizes at a constant level, indicative of a balance between the first and second transfers of the \*OH intermediate. Moreover, the absorption peak at 1367 cm<sup>-1</sup>, belonging to the stretching vibration of the C=O bond ( $\delta_{\text{C=O}}$ ) in EG, shows a significant increase intensity before 1.2 V, manifesting the substantial production of EG. However, the adsorption peak does not intensify significantly when further increasing the applied potential, suggesting an equilibrium between the formation of \*OHCH<sub>2</sub>CH<sub>2</sub>OH and the desorption of the formed EG, which could also be attested by the spectra at a constant potential of 1.4 V over time (Fig. S27). Importantly, no adsorption peaks, ascribing to the C=O bond, are observed during the electrolysis process, indicative of no formation of ethanoic acid or formic acid, further explaining the reason of 100% selectively for EG on Ir<sub>0.54</sub>Ru<sub>0.46</sub> catalyst. Through the analysis of *in-situ* ATR-FTIR spectra, we have gained the comprehensive insights into the process of electrooxidation of ethylene to EG, involving the activation of ethylene, H<sub>2</sub>O dissociation to \*OH, two \*OH transfer to couple with \*CH<sub>2</sub>CH<sub>2</sub> and the desorption of \*OHCH<sub>2</sub>CH<sub>2</sub>OH, as illustrated in Fig. 3(e).

To reveal the underlying enhancement mechanism of performance and selectivity on Ir<sub>0.54</sub>Ru<sub>0.46</sub> electrode toward ethylene to EG, we performed the density functional theory (DFT) calculation. A stable structural model of the Ru NPs and Ir<sub>0.54</sub>Ru<sub>0.46</sub> alloy was established (Fig. 4(a)). According to the

analysis of Bader charge (Fig. 4(b), Table S10), the introduction of Ir withdraws the electron from Ru and makes the Ru site positively charged, which is consistent with the results of XPS and XAS. Accordingly, the *d*-band center of IrRu downshifts from -1.643 to -1.732 eV (Fig. 4(c)), indicative of the weakened adsorption of \*OH, and \*CH<sub>2</sub>OHCH<sub>2</sub>OH after the introduction of Ir [43–45].

Fig. 4(d) represents the free energy changes of different reaction steps during the ethylene to EG conversion process. It is observed that the free energy of OH adsorption on Ru site is -1.26 eV in Ir<sub>0.54</sub>Ru<sub>0.46</sub>, which is 1.75 eV (Fig. 4(d)) higher than that of Ru NPs (-3.01 eV), again attesting the declined Ru-OH binding energy. Moreover, the coupling between \*OH and \*CH<sub>2</sub>CH<sub>2</sub> (S3) is the rate-determining step due to the highest energy barrier. Upon introduction of Ir, the energy barrier for the formation of \*CH<sub>2</sub>CH<sub>2</sub>OH intermediate dramatically decreases from 1.64 to 0.73 eV. Similarly, the energy barrier for the coupling of the second \*OH and desorption energy of \*HOCH<sub>2</sub>CH<sub>2</sub>OH also decreases from 0.93 to 0.27 eV and 0.86 to 0.68 eV, respectively. All these results provide the clear evidence to interpret the enhancement mechanism of EG formation after alloying with Ir. It is noting that, the first coupling of \*OH and \*CH<sub>2</sub>CH<sub>2</sub> (i.e., S2 → S3) is the rate-determining step for both pathway I and II on Ru NPs, implying that both EG and glycolic acid (GA) can be produced regardless of the energy barriers of subsequent steps. On the contrary, if the \*CH<sub>2</sub>CH<sub>2</sub>OH intermediate undergoes the continuous oxidation to \*CH<sub>2</sub>COOH (pathway II, S4), the calculated free energy is 1.1 eV, much higher than that of \*OHCH<sub>2</sub>CH<sub>2</sub>OH generation (pathway I, S4, 0.27 eV), demonstrating the thermodynamically favorable EG

formation rather than the subsequent peroxidation.

#### 4. Conclusions

In this work, we developed a novel Ru-based alloy catalyst that can convert ethylene to EG with 100% selectivity under the ambient condition. Advanced spectroscopies revealed that the introduction of Ir could decrease the electron density of Ru atoms and weaken the adsorption of \*OH adsorption, facilitating the formation of EG, which can also be verified by the DFT calculation. *In-situ* FT-IR further deciphered the reaction pathway and illuminated the enhancement mechanism in activity and selectivity. The optimized IrRu catalyst also showed the satisfactory durability with the stable productivity of ca. 6  $\mu\text{mol L}^{-1} \text{h}^{-1}$  along the 12 h electrolysis. This work provides new insight in the field of developing the electrocatalysts with high selectivity for the electrosynthesis of EG.

#### Declaration of Competing Interest

The authors declare that they have no known competing financial interest or personal relationship that could have appeared to influence the work reported in this paper.

#### Electronic supporting information

Supporting information is available in the online version of this article.

#### References

- [1] R. Geyer, J. R. Jambeck, K. L. Law, *Sci. Adv.*, **2017**, 3, e1700782.
- [2] H. R. Yue, Y. J. Zhao, X. B. Ma, J. L. Gong, *Chem. Soc. Rev.*, **2012**, 41, 4218–4244.
- [3] Y. F. Gao, L. Neal, D. Ding, W. Wu, C. Baroi, A. M. Gaffney, F. X. Li, *ACS Catal.*, **2019**, 9, 8592–8621.
- [4] Q. Yang, Q. C. Yang, S. M. Xu, S. Zhu, D. W. Zhang, *J. Cleaner Prod.*, **2020**, 273, 123120.
- [5] M. H. Guan, L. Y. Dong, T. Wu, W. C. Li, G. P. Hao, A. H. Lu, *Angew. Chem. Int. Ed.*, **2023**, 62, e202302466.
- [6] Y. Lum, J. E. Huang, Z. Y. Wang, M. C. Luo, D. H. Nam, W. R. Leow, B. Chen, J. Wicks, Y. G. C. Li, Y. H. Wang, C. T. Dinh, J. Li, T. T. Zhuang, F. W. Li, T. K. Sham, D. Sinton, E. H. Sargent, *Nat. Catal.*, **2020**, 3, 14–22.
- [7] T. M. Tang, Y. Wang, J. Y. Han, Q. Q. Zhang, X. Bai, X. D. Niu, Z. L. Wang, J. Q. Guan, *Chin. J. Catal.*, **2023**, 46, 48–55.
- [8] L. S. Xie, X. P. Zhang, B. Zhao, P. Li, J. Qi, X. N. Guo, B. Wang, H. T. Lei, W. Zhang, U. P. Apfel, R. Cao, *Angew. Chem. Int. Ed.*, **2021**, 60, 7576–7581.
- [9] Z. H. Li, X. F. Li, H. Zhou, Y. Xu, S. M. Xu, Y. Ren, Y. F. Yan, J. R. Yang, K. Y. Ji, L. Li, M. Xu, M. F. Shao, X. G. Kong, X. M. Sun, H. H. Duan, *Nat. Commun.*, **2022**, 13, 5009.
- [10] Y. X. Zhang, J. N. Li, N. Kornienko, *Cell Rep. Phys. Sci.*, **2021**, 2, 100682.
- [11] F. F. Xu, X. Liu, L. L. Zhang, M. X. Guo, M. Z. Li, X. Ding, L. X. Zhang, *Adv. Energy Mater.*, **2023**, 13, 2300615.
- [12] C. Han, B. B. Mei, Q. H. Zhang, H. M. Zhang, P. F. Yao, P. Song, X. Gong, P. X. Cui, Z. Jiang, L. Gu, W. L. Xu, *Chin. J. Catal.*, **2023**, 51, 80–89.
- [13] H. J. Li, Y. H. Xiao, J. L. Xiao, K. Fan, B. K. Li, X. L. Li, L. Wang, F. S. Xiao, *Chin. J. Catal.*, **2023**, 54, 178–187.
- [14] T. M. Tang, Z. L. Wang, J. Q. Guan, *Coord. Chem. Rev.*, **2023**, 492, 215288.
- [15] X. Peng, M. Zhang, H. Qin, J. Han, Y. Xu, W. Li, X. P. Zhang, W. Zhang, U. P. Apfel, R. Cao, *Angew. Chem. Int. Ed.*, **2024**, 63, e202401074.
- [16] L. L. Holbrook, H. Wise, *J. Catal.*, **1975**, 38, 294–298.
- [17] J. W. Ke, M. F. Chi, J. K. Zhao, Y. Liu, R. Y. Wang, K. Y. Fan, Y. X. Zhou, Z. K. Xi, X. D. Kong, H. L. Li, J. Zeng, Z. G. Geng, *J. Am. Chem. Soc.*, **2023**, 145, 9104–9111.

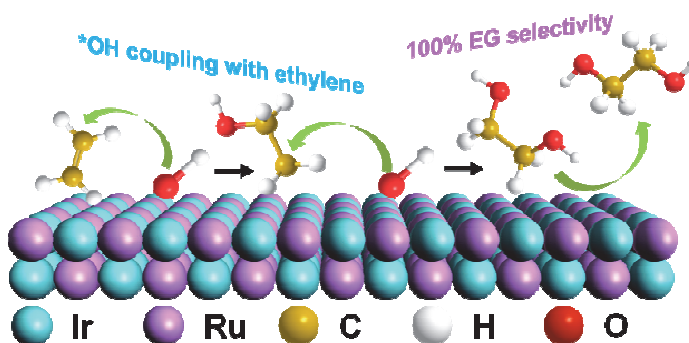
#### Graphical Abstract

*Chin. J. Catal.*, 2024, 60: 376–385 doi: 10.1016/S1872-2067(24)60024-0

#### Manipulating the electronic state of ruthenium to boost highly selective electrooxidation of ethylene to ethylene glycol in acid

Jie Wang, Yihe Chen, Yuda Wang, Hao Zhao, Jinyu Ye, Qingqing Cheng \*, Hui Yang \*

ShanghaiTech University; Shanghai Advanced Research Institute, Chinese Academy of Sciences; Xiamen University



The Ir-Ru alloy catalyst can efficiently catalyze the electrooxidation of ethylene to ethylene glycol with 100% selectivity and desirable durability in acidic medium.

- [18] X. W. Li, X. Y. You, Z. Yan, C. Y. Yang, L. L. Zuo, X. W. Huang, L. Chang, S. Y. Lu, Z. Y. Tang, *Mater. Chem. Front.*, **2023**, 7, 1437–1445.
- [19] W. R. Leow, Y. Lum, A. Ozden, Y. H. Wang, D. H. Nam, B. Chen, J. Wicks, T. T. Zhuang, F. W. Li, D. Sinton, E. H. Sargent, *Science*, **2020**, 368, 1228–1233.
- [20] X. Lin, Z. Y. Zhou, Q. Y. Li, D. Xu, S. Y. Xia, B. L. Leng, G. Y. Zhai, S. N. Zhang, L. H. Sun, G. H. Zhao, J. S. Chen, X. H. Li, *Angew. Chem. Int. Ed.*, **2022**, 61, e202207108.
- [21] J. S. Jirkovsky, M. Busch, E. Ahlberg, I. Panas, P. Krtil, *J. Am. Chem. Soc.*, **2011**, 133, 5882–5892.
- [22] J. K. Norskov, J. Rossmeisl, A. Logadottir, L. Lindqvist, J. R. Kitchin, T. Bligaard, H. Jónsson, *J. Phys. Chem. B*, **2004**, 108, 17886–17892.
- [23] A. Zagalskaya, V. Alexandrov, *ACS Catal.*, **2020**, 10, 3650–3657.
- [24] Y. C. Yao, S. L. Hu, W. X. Chen, Z. Q. Huang, W. C. Wei, T. Yao, R. R. Liu, K. T. Zang, X. Q. Wang, G. Wu, W. J. Yuan, T. W. Yuan, B. Q. Zhu, W. Liu, Z. J. Li, D. S. He, Z. G. Xue, Y. Wang, X. S. Zheng, J. C. Dong, C. R. Chang, Y. X. Chen, X. Hong, J. Luo, S. Q. Wei, W. X. Li, P. Strasser, Y. E. Wu, Y. D. Li, *Nat. Catal.*, **2019**, 2, 304–313.
- [25] Y. P. Liu, X. Liang, H. Chen, R. Q. Gao, L. Shi, L. Yang, X. X. Zou, *Chin. J. Catal.*, **2021**, 42, 1054–1077.
- [26] L. Y. Xiao, L. L. Qi, J. R. Sun, A. Husile, S. Y. Zhang, Z. L. Wang, J. Q. Guan, *Nano Energy*, **2024**, 120, 109155.
- [27] X. Bai, J. Y. Han, S. Y. Chen, X. D. Niu, J. Q. Guan, *Chin. J. Catal.*, **2023**, 54, 212–219.
- [28] H. Y. Lv, X. P. Zhang, K. Guo, J. X. Han, H. B. Guo, H. T. Lei, X. L. Li, W. Zhang, U. P. Apfel, R. Cao, *Angew. Chem. Int. Ed.*, **2023**, 62, e202305938.
- [29] L. C. Seitz, C. F. Dickens, K. Nishio, Y. Hikita, J. Montoya, A. Doyle, C. Kirk, A. Vojvodic, H. Y. Hwang, J. K. Norskov, T. F. Jaramillo, *Science*, **2016**, 353, 1011–1014.
- [30] P. Lettenmeier, L. Wang, U. Golla-Schindler, P. Gazdzicki, N. A. Cañas, M. Handl, R. Hiesgen, S. S. Hosseiny, A. S. Gago, K. A. Frie-  
rich, *Angew. Chem. Int. Ed.*, **2016**, 55, 742–746.
- [31] X. B. Zheng, J. R. Yang, Z. F. Xu, Q. S. Wang, J. B. Wu, E. H. Zhang, S. X. Dou, W. P. Sun, D. S. Wang, Y. D. Li, *Angew. Chem. Int. Ed.*, **2022**, 61, e202205946.
- [32] H. H. You, D. S. Wu, D. H. Si, M. N. Cao, F. F. Sun, H. Zhang, H. M. Wang, T. F. Liu, R. Cao, *J. Am. Chem. Soc.*, **2022**, 144, 9254–9263.
- [33] C. C. Dai, Y. M. Sun, G. Chen, A. C. Fisher, Z. C. J. Xu, *Angew. Chem. Int. Ed.*, **2020**, 59, 9418–9422.
- [34] C. X. Li, Q. Q. Cheng, C. Y. Wu, Q. S. Wang, W. B. Hu, L. L. Zou, K. Wen, H. Yang, *Chem. Commun.*, **2022**, 58, 10496–10499.
- [35] S. Garcia-Segura, F. Centellas, E. Brillas, *J. Phys. Chem. C*, **2012**, 116, 15500–15504.
- [36] K. Hu, P. Zhou, Y. Yang, T. Hall, G. Nie, Y. Yao, X. Duan, S. Wang, *ACS EST Engg.*, **2021**, 2, 110–120.
- [37] J. W. Ke, J. K. Zhao, M. F. Chi, M. L. Wang, X. D. Kong, Q. X. Chang, W. R. Zhou, C. X. Long, J. Zeng, Z. G. Geng, *Nat. Commun.*, **2022**, 13, 932.
- [38] J. S. Wang, S. S. Xin, Y. Xiao, Z. F. Zhang, Z. M. Li, W. Zhang, C. J. Li, R. Bao, J. Peng, J. H. Yi, S. L. Chou, *Angew. Chem. Int. Ed.*, **2022**, 61, e202202518.
- [39] S. Zhang, P. Kang, T. J. Meyer, *J. Am. Chem. Soc.*, **2014**, 136, 1734–1737.
- [40] H. W. Huang, H. H. Jia, Z. Liu, P. F. Gao, J. T. Zhao, Z. L. Luo, J. L. Yang, J. Zeng, *Angew. Chem. Int. Ed.*, **2017**, 56, 3594–3598.
- [41] L. B. Xie, P. F. Wang, Y. Li, D. P. Zhang, D. H. Shang, W. W. Zheng, Y. G. Xia, S. H. Zhan, W. P. Hu, *Nat. Commun.*, **2022**, 13, 5560.
- [42] H. S. Wang, H. D. Abruna, *J. Am. Chem. Soc.*, **2023**, 145, 18439–18446.
- [43] S. Q. Zhu, X. P. Qin, F. Xiao, S. L. Yang, Y. Xu, Z. Tan, J. D. Li, J. W. Yan, Q. Chen, M. S. Chen, M. H. Shao, *Nat. Catal.*, **2021**, 4, 711–718.
- [44] L. Y. Xiao, Z. L. Wang, J. Q. Guan, *Chem. Sci.*, **2023**, 14, 12850–12868.
- [45] L. Y. Xiao, Z. L. Wang, J. Q. Guan, *Adv. Funct. Mater.*, **2024**, 34, 2310195.

## 调控Ru的电子态以促进乙烯在酸中高选择性电氧化合成乙二醇

王杰<sup>a,b</sup>, 陈怡和<sup>a,b</sup>, 王宇达<sup>b</sup>, 赵浩<sup>b</sup>, 叶进裕<sup>c</sup>, 程庆庆<sup>b,\*</sup>, 杨辉<sup>a,b,\*</sup>

<sup>a</sup>上海科技大学物质科学与技术学院, 上海201210

<sup>b</sup>中国科学院上海高等研究院, 上海201210

<sup>c</sup>厦门大学化学化工学院, 福建厦门361005

**摘要:** 乙二醇(EG)是一种重要的化工产品, 由于在化学品制造行业的广泛应用而备受关注。然而, 目前工业上制备乙二醇主要采用乙烯作为原料, 经过环氧化和水解两步反应, 这一过程不仅需要高温高压, 还需使用成本高的氧化剂(如H<sub>2</sub>O<sub>2</sub>), 这违背了绿色化学的原则。因此, 电催化阳极氧化作为一种新兴的合成策略, 正逐渐受到研究者的青睐。该技术仅通过电子转移并利用水作为氧源, 就能够高效合成高附加值含氧化学品。特别是, 阳极氧化反应可与阴极还原反应(例如氢析出反应)相耦合, 实现能量的高效利用。尽管电催化阳极氧化具有诸多优势, 但目前在乙烯电氧化合成乙二醇过程中, 其选择性仍然较低, 这导致后续的纯化过程变得复杂且成本高昂。因此, 开发高选择性的电氧化合成乙二醇技术, 成为了一项迫切且极具挑战性的任务。

本文提出了一种Ir和Ru合金化策略, 以提高乙烯电氧化制备乙二醇的选择性和耐久性。研究结果表明, 当Ir和Ru的原子比达到适当的比例(即Ir<sub>0.54</sub>Ru<sub>0.46</sub>)时, 所制备的IrRu合金表现出近100%的乙二醇选择性, 远远优于Ru NPs对照组样品(43.8%)。此外, 在1.475 V的电压下, Ir<sub>0.54</sub>Ru<sub>0.46</sub>催化生成乙二醇产率达到了60.62 mmolg<sub>Ru</sub><sup>-1</sup> h<sup>-1</sup>, 是Ru NPs上最高产率(21.75 mmolg<sub>Ru</sub><sup>-1</sup> h<sup>-1</sup>)的2.8倍。在耐久性测试中, Ir<sub>0.54</sub>Ru<sub>0.46</sub>能够稳定催化生成乙二醇超过12 h, 其生成速率为6 μmol L<sup>-1</sup> h<sup>-1</sup>。相比之下, 对照组样品Ru NPs在电解反应3 h后已失去活性。能量损失谱分析显示, Ir<sub>0.54</sub>Ru<sub>0.46</sub>在电解2 h后形成了稳定的表面富Ir核壳结构IrRu@Ir, 这是催化剂稳定性提升的关键。先进光谱研究进一步揭示, Ir的引入导致了电子由Ru位点向Ir流动, 使Ru位点带正电荷, 从而减弱了OH的吸附。OH脱附实验结果表明, 随着Ir/Ru原子比的增加, OH更容易从Ru位点脱附, 这促进

了OH与乙烯的偶联反应。自由基淬灭和氘代同位素标记实验结果表明,在IrRu催化剂上,乙烯到乙二醇的转化并非级联反应,而是直接的表面催化反应,其中OH的转移是决速步骤。X射线光电子能谱分析显示,随着合金中Ir比例的增加,合金d带中心下移,这有利于关键中间体(\*OH等)的转移。原位红外光谱表明,乙烯分子在Ru位点上通过Pauling型吸附构型被活化。值得注意的是,仅检测到\*CH<sub>2</sub>CH<sub>2</sub>OH中间体,而未检测到其他氧基团(如羰基),这表明在反应过程中没有发生过氧化现象。密度泛函理论计算进一步证实,与Ir合金化不仅加速了OH的转移,还优化了反应途径,使乙二醇的选择性达到100%。

综上,本文设计了不同Ir/Ru原子比的IrRu合金催化剂,通过有效调控活性位点Ru的电子结构,优化了OH的结合能,使乙烯可以100%选择性高效转化为乙二醇,这为开发高选择性电催化剂用于乙二醇电合成提供了新思路。

**关键词:** 乙烯电氧化; 电合成乙二醇; 高选择性; IrRu合金; 电子结构

收稿日期: 2024-01-26. 接受日期: 2024-03-26. 上网时间: 2024-05-20.

\*通讯联系人. 电子邮箱: chengqq@sari.ac.cn (程庆庆), yangh@sari.ac.cn (杨辉).

基金来源: 国家重点研发计划(2021YFB4000200); 上海市自然科学基金面上项目(23ZR1471000).